



**HAL**  
open science

# Tuning the emission color and temperature range of dual-mode luminescent thermometer by dopant valence states control

Estelle Glais, Florian Massuyeau, Romain Gautier

► **To cite this version:**

Estelle Glais, Florian Massuyeau, Romain Gautier. Tuning the emission color and temperature range of dual-mode luminescent thermometer by dopant valence states control. *Applied Materials Today*, 2022, 26, pp.101349. 10.1016/j.apmt.2021.101349 . hal-03666523

**HAL Id: hal-03666523**

**<https://hal.science/hal-03666523>**

Submitted on 25 Oct 2022

**HAL** is a multi-disciplinary open access archive for the deposit and dissemination of scientific research documents, whether they are published or not. The documents may come from teaching and research institutions in France or abroad, or from public or private research centers.

L'archive ouverte pluridisciplinaire **HAL**, est destinée au dépôt et à la diffusion de documents scientifiques de niveau recherche, publiés ou non, émanant des établissements d'enseignement et de recherche français ou étrangers, des laboratoires publics ou privés.

# Tuning the Emission Color and Temperature Range of Dual-mode Luminescent Thermometer by Dopant Valence States Control

Estelle Glais<sup>1\*</sup>, Florian Massuyeau<sup>1</sup>, Romain Gautier<sup>1\*</sup>

<sup>1</sup> Université de Nantes, CNRS, Institut des Matériaux Jean Rouxel (IMN), F-44000 Nantes, France

\*Corresponding authors: [estelle.glais@cnrs-immn.fr](mailto:estelle.glais@cnrs-immn.fr) and [romain.gautier@cnrs-immn.fr](mailto:romain.gautier@cnrs-immn.fr)

## Abstract

Dual emitting materials are of great interest for luminescence thermometry. The operating temperature range, the thermal sensitivity as well as the emission color are crucial parameters, which define the competitiveness of the thermal sensor. In this work, we propose a new and convenient method for the modulation of emission color range and sensitivity through the control of the dopant oxidation states and crystal field variations. To this end, we investigated inorganic phosphors in which two valence states of Mn luminescent centers can be stabilized. When inserted in octahedral environment, Mn<sup>4+</sup> ions present a red luminescence ( ${}^2E \rightarrow {}^4A_2$  transition), whereas Mn<sup>2+</sup> ions exhibit a green luminescence in tetrahedral environment ( ${}^4T_1 \rightarrow {}^6A_1$  transition). Due to the different behavior of Mn<sup>4+</sup> and Mn<sup>2+</sup> luminescence properties according to the temperature, the resulting emission color vary from red to green and can be exploited for visual temperature detection. We demonstrate the proportion of Mn<sup>4+</sup> and Mn<sup>2+</sup> ions can be finely tuned, owing to a thermally driven Mn<sup>4+</sup> to Mn<sup>2+</sup> reduction, which allow to modulate color change at a specific temperature. Two isostructural materials were investigated SrMgAl<sub>10</sub>O<sub>17</sub>:Mn<sup>4+</sup>,Mn<sup>2+</sup> and BaMgAl<sub>10</sub>O<sub>17</sub>:Mn<sup>4+</sup>,Mn<sup>2+</sup> and can be envisioned as competitive ratiometric and colorimetric luminescent thermometer, with tunable properties.

## Keywords

Luminescent sensors ; dopant valence state ; Mn luminescent centers ; dual-mode thermometer

## 1. Introduction

Luminescence thermometry is a promising method that have been extensively studied over the past decade [1], which allows a precise, real time, and contactless measurement of the temperature. Thermometry based on luminescence properties changes of materials is relevant in various fields as medicine, aeronautic, microfluidic or catalysis [2–4]. The accuracy as well as the temperature range, on which the luminescent sensor should be efficient, vary according to the selected application. Numerous inorganic materials doped with luminescent ions have been developed and are very

promising [5–7]. The robustness and the competitiveness of a specific luminescent sensor can be defined thanks to its thermal sensitivity. However, the tuning of the temperature ranges in which the material sensitivity reaches the maximal value, as well as the modulation of the resulting emission color at a given temperature remains challenging. The lack of properties flexibility of specific materials with remarkable performances for thermal sensing limit their development to other applications. As a consequence, a variety of materials with targeted features is needed. In this work, we propose a new and simple method for the thermal response modulation of a single luminescent material. More specifically, we focus on the stabilization of several valence states of the same element, namely  $\text{Mn}^{4+}$  and  $\text{Mn}^{2+}$  (the two main existing forms of Mn ions studied for their luminescence properties), in a single matrix. Manganese is an abundant resource, and can be considered as an efficient alternative to rare earth elements for luminescence applications. The local coordination as well as the distribution in the host lattice determines the luminescence properties of divalent or tetravalent Mn ions [8]. The photoluminescence color of  $\text{Mn}^{2+}$  ion varies from green to red according to the local environment in which it is inserted whereas  $\text{Mn}^{4+}$  ion exhibits a red emission [9–11]. Moreover,  $\text{Mn}^{4+}$  doped-materials have been of interest for luminescence thermometry application [12–15]. The difference in the luminescence thermal sensitivity between  $\text{Mn}^{4+}$  and  $\text{Mn}^{2+}$  ions has recently been reported in some inorganic materials [16,17]. The co-stabilization of  $\text{Mn}^{2+}$  and  $\text{Mn}^{4+}$  ions in two isostructural materials, namely  $\text{SrMgAl}_{10}\text{O}_{17}:\text{Mn}^{4+},\text{Mn}^{2+}$  (SMA:Mn) and  $\text{BaMgAl}_{10}\text{O}_{17}:\text{Mn}^{4+},\text{Mn}^{2+}$  (BMA:Mn) has been discussed. In such matrices,  $\text{Mn}^{2+}$  and  $\text{Mn}^{4+}$  ions are stabilized in tetrahedral and octahedral sites respectively leading to two distinct emission bands [18–25]. Using an approach similar to the one previously implemented for  $\text{Eu}^{3+}/\text{Eu}^{2+}$  doped oxides in solid state lighting applications [26,27], we selected SMA and BMA materials to precisely control the reduction process of  $\text{Mn}^{4+}$  to  $\text{Mn}^{2+}$  and the corresponding luminescence properties. SMA:Mn and BMA:Mn are investigated as colorimetric and ratiometric dual-mode luminescent thermometer. The dopant valence state is demonstrated as efficient parameter for the modulation of the color range as well as the associated temperature.

## 2. Material & Methods

$\text{SrMgAl}_{10}\text{O}_{17}:\text{Mn}$  and  $\text{BaMgAl}_{10}\text{O}_{17}:\text{Mn}$  materials were prepared through a solid state synthesis.  $\text{SrCO}_3$ ,  $\text{BaCO}_3$ ,  $\text{MgO}$ ,  $\text{Al}_2\text{O}_3$ ,  $\text{MnCO}_3$  were used as starting materials. Precursors were weighted according to stoichiometric proportions and grounded in agate mortar during 30 min. Only  $\text{MgO}$  precursor was incorporated in excess to improve  $\text{Mn}^{4+}$  stabilization (charge compensation) and to prevent the formation of the parasitic phases  $\text{SrAl}_2\text{O}_4$  and  $\text{BaAl}_2\text{O}_4$ . The as prepared powder was transferred to alumina crucible and heated at 1500 °C during 15 h. This sintering process was performed under air using a muffle furnace and repeated in order to reduce the proportion of secondary phases. The crystallized materials were then placed in a home-made machined stumatite

sample holder where several isolated crucibles are continuously distributed along the temperature gradient axis. This sample holder was placed in a thermal gradient oven under ultra-high vacuum ( $\approx 10^{-6}$  mbar) for the reductive thermal treatment (temperature range from 400 °C to 800 °C, SI - 3). X-ray diffraction patterns were obtained by powder X-ray diffraction using a Bruker D8 diffractometer with Cu-K $\alpha$  radiation ( $\lambda = 1.5406$  Å). Diffraction data were recorded in a  $2\theta$  range from 10° to 90° in 0.02° steps. Excitation and emission photoluminescence spectra were recorded with a Jobin-Yvon Fluorolog 3 spectrophotometer using a xenon light source (450 W). Liquid nitrogen cryostat Oxford OptistatDN-V was used for temperature dependent photoluminescence spectra.

### 3. Results and discussion

#### 3.1. Crystal structure and phase identification

SMA:Mn and BMA:Mn materials both present isostructural crystal structures ( $P6_3/mmc$  space group). SMA:Mn and BMA:Mn exhibit an orderly layered structure in which spinel blocks of  $MgAl_{10}O_{16}$  are separated by SrO or BaO planes. Both SMA and BMA structures exhibit octahedral and tetrahedral sites in which  $Mn^{4+}$  and  $Mn^{2+}$  ions can be respectively inserted. According to ionic radii consideration, it can be assumed that  $Mn^{4+}$  ( $r = 53$  pm) ions are preferentially stabilized in  $[AlO_6]$  sites ( $r = 53.5$  pm) whereas  $Mn^{2+}$  ions ( $r = 66$  pm) substitute  $Mg^{2+}$  ions ( $r = 57$  pm) in tetrahedral sites. XRD patterns are represented in Figure 1.  $SrMgAl_{10}O_{17}$  and  $BaMgAl_{10}O_{17}$  phases can be clearly observed, corresponding to PDF 89-0572 and PDF 84-0818 respectively.  $SrAl_2O_4$  and  $BaAl_2O_4$  impurities can also be identified (represented by stars on the XRD patterns Figure 1). In order to

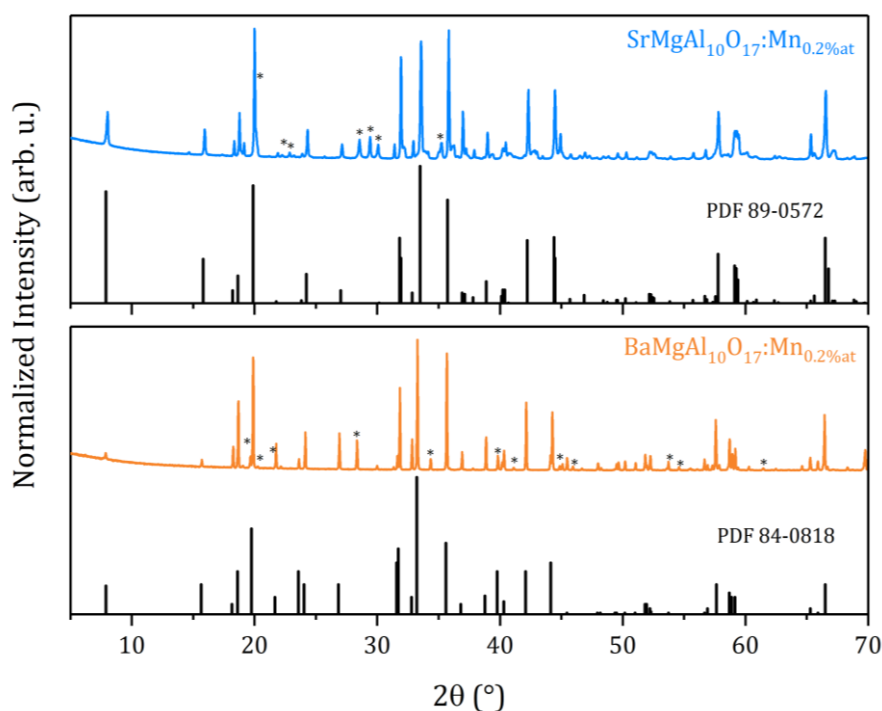


Figure 1 : XRD patterns of  $SrMgAl_{10}O_{17}:Mn_{0.2\%at}$  (blue) and  $BaMgAl_{10}O_{17}:Mn_{0.2\%at}$  (orange)

reduce the proportion of SrAl<sub>2</sub>O<sub>4</sub> and BaAl<sub>2</sub>O<sub>4</sub> secondary phases, MgO precursor are introduced in excess and the sintering process is repeated 3 times (SI - 1). Due to the small proportion of the SrAl<sub>2</sub>O<sub>4</sub> and BaAl<sub>2</sub>O<sub>4</sub> phases as reported in Table SI - 2, and the absence of Mn<sup>4+</sup> luminescence signal originating from these secondary phases, it is assumed that no change in the luminescence properties is induced by the presence of these impurities.

### 3.2. Optical characterizations

Emission spectra of SMA:Mn and BMA:Mn are reported in Figure 2a. Two emission bands can be identified. The first band centered at 514 nm can be attributed to the <sup>4</sup>T<sub>1</sub> → <sup>6</sup>A<sub>1</sub> transition of Mn<sup>2+</sup> ion. The second one centered around 660 nm corresponds to the <sup>2</sup>E → <sup>4</sup>A<sub>2</sub> (Mn<sup>4+</sup>) transition. Excitation spectra monitored at 514 nm and 658/660 nm are characteristic of Mn<sup>2+</sup> and Mn<sup>4+</sup> signatures respectively (Figure 2b). Four bands can be highlighted in Mn<sup>2+</sup> excitation spectra, the corresponding transitions

<sup>6</sup>A<sub>1</sub> → <sup>4</sup>T<sub>2</sub> (<sup>4</sup>G), <sup>6</sup>A<sub>1</sub> → <sup>4</sup>E, <sup>4</sup>A<sub>1</sub> (<sup>4</sup>G), <sup>6</sup>A<sub>1</sub> → <sup>4</sup>T<sub>2</sub> (<sup>4</sup>D), and <sup>6</sup>A<sub>1</sub> → <sup>4</sup>E (<sup>4</sup>D) are reported in the schematic scheme of energy level (Figure 2c). Both activators can be excited in the blue and in the UV regions. Similarly, three bands can be identified on Mn<sup>4+</sup> excitation spectra. They can be attributed to the <sup>4</sup>A<sub>2</sub> → <sup>4</sup>T<sub>1</sub>, <sup>4</sup>A<sub>2</sub> → <sup>2</sup>T<sub>2</sub> and <sup>4</sup>A<sub>2</sub> → <sup>4</sup>T<sub>2</sub> transitions. In addition, the excitation spectrum of Mn<sup>4+</sup> inserted in BaMgAl<sub>10</sub>O<sub>17</sub> host matrix is blue shifted compared to excitation spectrum of Mn<sup>4+</sup> inserted in SrMgAl<sub>10</sub>O<sub>17</sub>. As a d<sup>3</sup> ion, the position of Mn<sup>4+</sup> energy levels depends on the environment in which it is inserted. The corresponding Tanabe Sugano diagram is reported in Figure 2d. The relative position of energy levels involved in the photoluminescence process is drastically dependant on the crystal field strength (Dq) and on the interelectronic interaction represented by the Racah parameter B. The Dq/B value of both SMA:Mn and BMA hosts are reported on the Tanabe-Sugano diagram [28,29]. It can clearly be highlighted that a Sr<sup>2+</sup> by Ba<sup>2+</sup> substitution in isostructural host leads to an important variation of the energy of the <sup>4</sup>T<sub>1</sub> and <sup>4</sup>T<sub>2</sub> levels compared to the <sup>2</sup>E and <sup>4</sup>A<sub>2</sub> levels. Such a difference can be directly observed on excitation spectra, the energy increase between levels involved in radiative transition leads to a blue shift of the associated bands. As a consequence, the spectral overlap between Mn<sup>2+</sup> emission spectrum and Mn<sup>4+</sup> excitation spectrum is smaller in BMA compared to SMA host. Excitation wavelengths are selected in order to optimize Mn<sup>4+</sup> and Mn<sup>2+</sup> emissions and are fixed at 426 nm for SMA:Mn samples and 450 nm for BMA:Mn samples for this work.

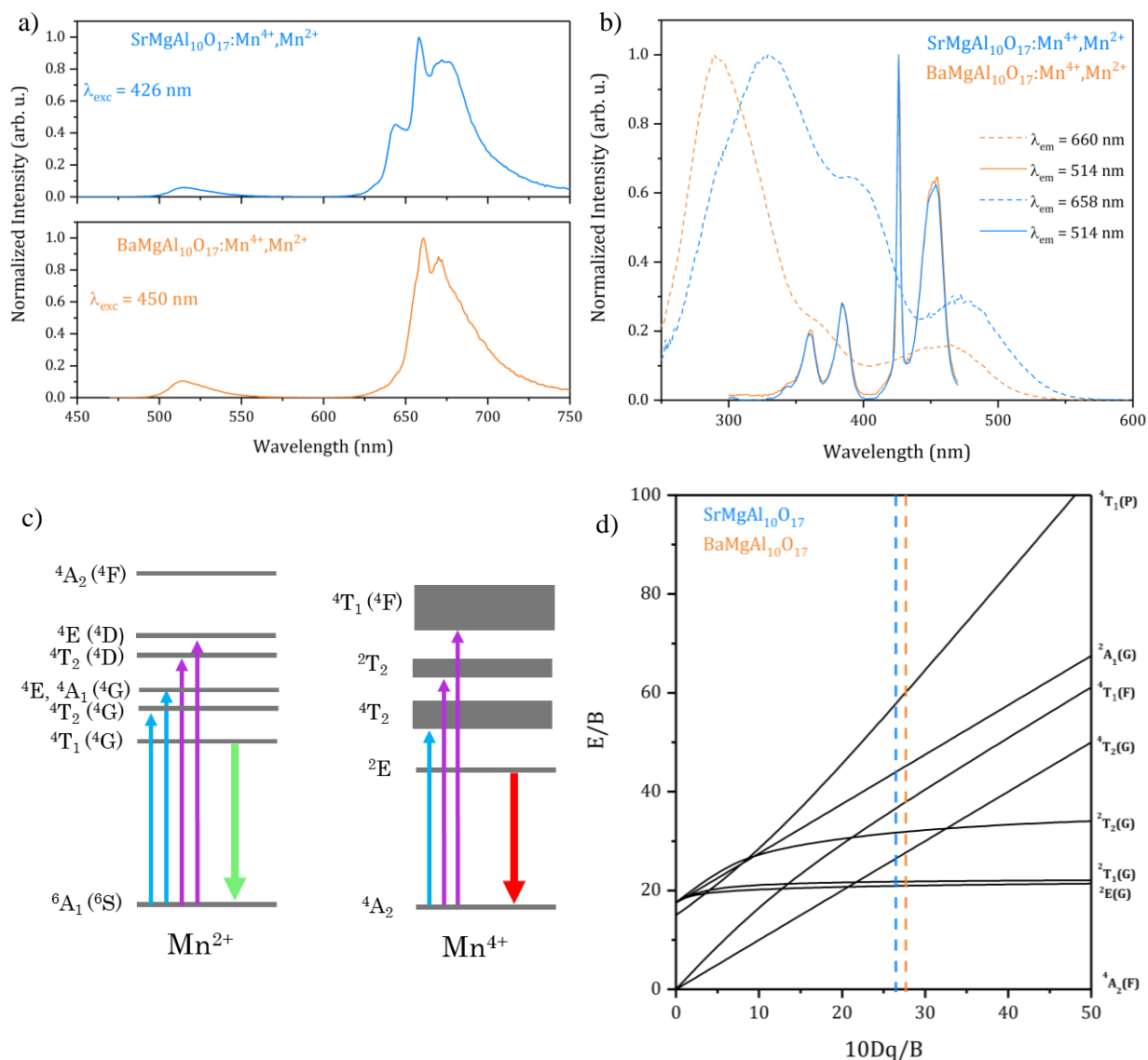


Figure 2 : a) Emission spectra of  $\text{SrMgAl}_{10}\text{O}_{17}:\text{Mn}^{4+},\text{Mn}^{2+}$  (blue) and  $\text{BaMgAl}_{10}\text{O}_{17}:\text{Mn}^{4+},\text{Mn}^{2+}$  (orange) b) Excitation spectra of  $\text{SrMgAl}_{10}\text{O}_{17}:\text{Mn}^{4+},\text{Mn}^{2+}$  (blue) and  $\text{BaMgAl}_{10}\text{O}_{17}:\text{Mn}^{4+},\text{Mn}^{2+}$  (orange), the dashed lines (resp. solid lines) correspond to  $\text{Mn}^{4+}$  (resp.  $\text{Mn}^{2+}$ ) excitation spectra c) schematic representation of  $\text{Mn}^{2+}$  and  $\text{Mn}^{4+}$  energy levels and the corresponding transitions observed in photoluminescence spectra d) Tanabe-Sugano diagram of  $d^3$  ion in octahedral environment; the blue (resp. orange) dashed line corresponds to the crystal field strength of  $\text{SrMgAl}_{10}\text{O}_{17}$  (resp. of  $\text{BaMgAl}_{10}\text{O}_{17}$ ) host matrix.

### 3.3. Modulation of $\text{Mn}^{4+}/\text{Mn}^{2+}$ ratio

The co-stabilisation of  $\text{Mn}^{4+}$  and  $\text{Mn}^{2+}$  ions in SMA and BMA hosts after synthesis in air atmosphere has been highlighted through the analysis of photoluminescence properties. The  $\text{Mn}^{4+}/\text{Mn}^{2+}$  ratio can be modulated owing to a reductive thermal treatment (RTT) of samples after synthesis. To this end, a thermal gradient oven is used, which allows to perform the reductive

treatment at several temperatures in a single experiment. Thirteen samples are post-treated at the same time under ultra-high vacuum along the temperature gradient (from 400 °C to 800 °C). No significant change in the XRD patterns is observed before and after the reductive thermal treatment. Rietveld refinements before and after reductive thermal treatment are reported in SI - 2, indicating that the RTT has neither influence on the crystal structure nor on the purity of the samples.

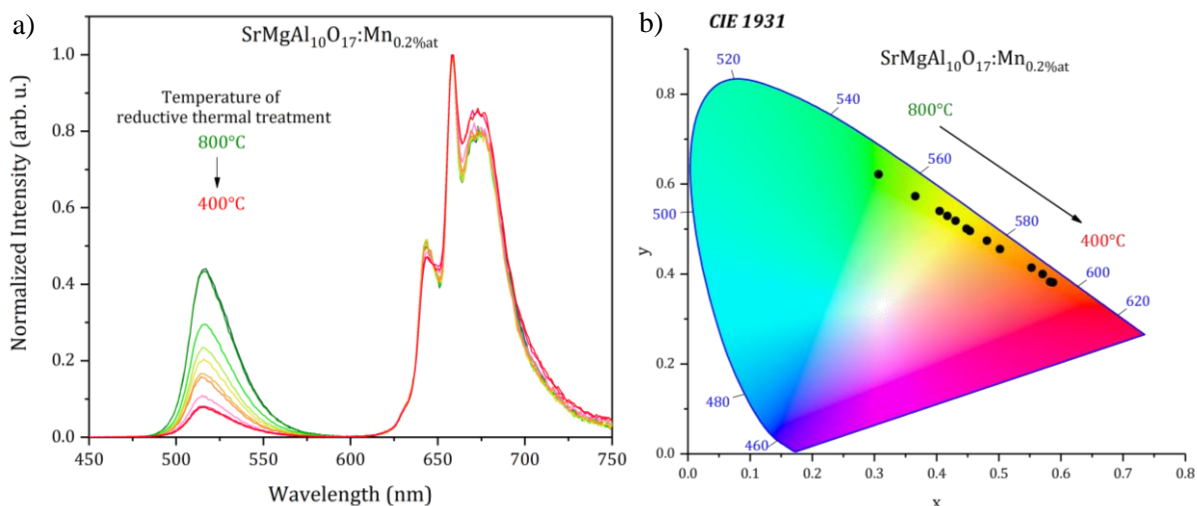


Figure 3 : a) Photoluminescence spectra of SrMgAl<sub>10</sub>O<sub>17</sub>:Mn<sup>4+</sup>,Mn<sup>2+</sup> after reductive thermal treatment at different temperatures from 400 °C (dark green) to 800 °C (red) –  $\lambda_{exc} = 426$  nm b) associated CIE coordinates.

To accelerate the characterization process, we designed a set up to collect photoluminescence properties directly on the stumatite sample holder, without further sample handling (SI - 3). The sample holder is fixed on a X-Y table in which the movement along two axes is computer-controlled. Optical fibers are coupled to the spectrofluorimeter. Each sample is characterized by automatically moving the sample holder along X and Y axes. The recorded photoluminescence spectra are presented in Figure 3a. The intensity of Mn<sup>2+</sup> emission increases relatively to Mn<sup>4+</sup> emission when the temperature of the RTT increases. Thus the RTT allows the increase of Mn<sup>2+</sup> concentration due to the progressive reduction of Mn<sup>4+</sup> into Mn<sup>2+</sup>. As the Mn<sup>2+</sup> emission band is characteristic of Mn<sup>2+</sup> ion in tetrahedral site, we assume that the reduction process is associated with cation diffusion from Oh site to Td site. The charge balance would be preserved owing to the formation of oxygen vacancies. The resulting emission color associated to each photoluminescence spectra are presented on CIE diagram Figure 3b. The color emission shifts from red to green with the increase of RTT temperature. After a RTT at 800 °C under ultra-high vacuum, the Mn<sup>4+</sup> emission band is still detected as the reduction of Mn<sup>4+</sup> → Mn<sup>2+</sup> is not complete. However, since the human eyes are more sensitive to green light, the proportion of Mn<sup>2+</sup> is sufficient to shift the resulting emission color in the green region. The same phenomenon is obtained for BMA material (SI - 4). This method, based on the thermally-driven reduction of dopant, enables the fast synthesis of a large number of compounds. It allows the fine

tuning of the oxidation state of dopants and the modulation of the luminescence properties. The same approach can be transposed to many other systems for the discovery of new materials with competitive and flexible properties.

### 3.4. Luminescence thermometry

The luminescence behavior according to the temperature is then investigated on samples with fixed  $\text{Mn}^{4+}$  and  $\text{Mn}^{2+}$  concentrations. The photoluminescence spectra of  $\text{SrMgAl}_{10}\text{O}_{17}:\text{Mn}^{4+},\text{Mn}^{2+}$  after reductive thermal treatment with resulting yellow-orange emission ( $T_{\text{RTT}} \approx 750\text{ }^{\circ}\text{C}$ ) are recorded from  $0\text{ }^{\circ}\text{C}$  to  $200\text{ }^{\circ}\text{C}$  (Figure 4a). The selected sample is labeled as SMA-RTT. In the investigated temperature range, the intensity of  $\text{Mn}^{2+}$  band only slightly decreases compared to the  $\text{Mn}^{4+}$  contribution. To this end,  $\text{Mn}^{2+}$  will be considered as the reference. As reported in Figure 4b, the  $\text{Mn}^{4+}$   ${}^2\text{E} \rightarrow {}^4\text{A}_2$  transition exhibits a huge temperature dependence. The evolution of  $\text{Mn}^{4+}/\text{Mn}^{2+}$  intensity ratio according to the temperature is reported Figure 5 and can be modeled by a sigmoidal curve as the emission arises from two distinct emitting centers. The investigated temperature range is smaller than the temperature required for  $\text{Mn}^{4+}$  reduction into  $\text{Mn}^{2+}$ . We assume that concentrations of both ions remain constant on this whole range. Consequently, this parameter is not responsible of the luminescence properties variation according to the temperature.

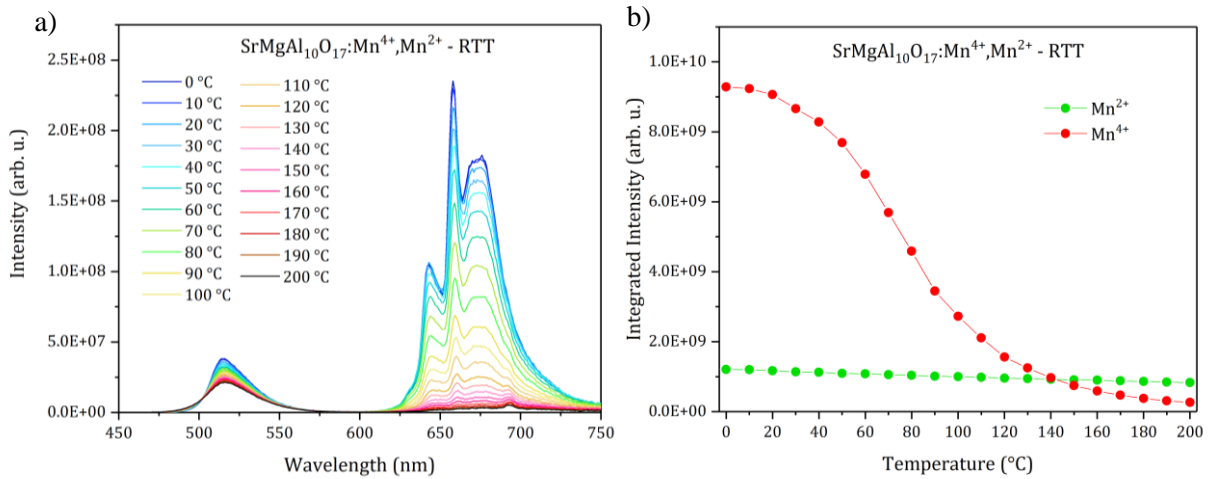


Figure 4 : a) Photoluminescence spectra of  $\text{SrMgAl}_{10}\text{O}_{17}:\text{Mn}^{4+},\text{Mn}^{2+}$ -RTT from 0 to  $200\text{ }^{\circ}\text{C}$  b) associated integrated intensity of  $\text{Mn}^{4+}$  (red) and  $\text{Mn}^{2+}$  (green) bands.

The competition between radiative and non-radiative deexcitation process can be modelled by Mott-Seitz function (Equation 1), where  $k_B$  is the Boltzmann constant,  $\Delta E$  the activation energies of thermal quenching process,  $I_0$  the intensity emission at  $T = 0\text{ K}$ , and  $a$  a fitting parameter corresponding to the ratio between radiative and non-radiative transition probabilities [30]. In this general equation, all deactivation channels that can be induced by the temperature increase are taken into account.



$$\frac{I_{Mn^{4+}}}{I_{Mn^{2+}}} = \frac{I_{Mn^{4+0}}}{I_{Mn^{2+0}}} \frac{\sum_i (1 + a_{Mn^{2+i}} \exp(\frac{-\Delta E_{Mn^{2+i}}}{k_B T}))}{\sum_j (1 + a_{Mn^{4+j}} \exp(\frac{-\Delta E_{Mn^{4+j}}}{k_B T}))} \quad (1)$$

However, in the case of SrMgAl<sub>10</sub>O<sub>17</sub>:Mn<sup>4+</sup>,Mn<sup>2+</sup>-RTT sample, Mn<sup>4+</sup> exhibits a greater temperature dependence than Mn<sup>2+</sup> in the investigated temperature range, thus the Mn<sup>2+</sup> contribution can be neglected. In addition, only one quenching process is identified, therefore one deexcitation channel (indexed channel 1) can be considered. Thus, the fitting equation is simplified (see Equation 2) and the associated fitting curve can be plotted (dashed line in Figure 5) with the following fitting parameters I<sub>0</sub> = 8.22 ± 0.11, a<sub>1</sub> = 2.96 10<sup>6</sup> ± 1.58 10<sup>6</sup>, and ΔE<sub>1</sub> = 3696 ± 139 cm<sup>-1</sup>.

$$\frac{I_{Mn^{4+}}}{I_{Mn^{2+}}} \simeq I_0 \frac{1}{1 + a_1 \exp(\frac{-\Delta E_1}{k_B T})} \quad (2)$$

The thermal sensitivity, defined by Equation 3, is represented in solid blue line on Figure 5. In the case of SMA-RTT material, the thermal sensitivity value increases from RT to 130°C to reach 2.77 %/°C, and then slowly decreases when the temperature is further stepped up. The sensitivity is competitive compared to other luminescent thermometer reported in the literature [3,31,32], which confirm the ability of SMA:Mn material as effective ratiometric thermometer.

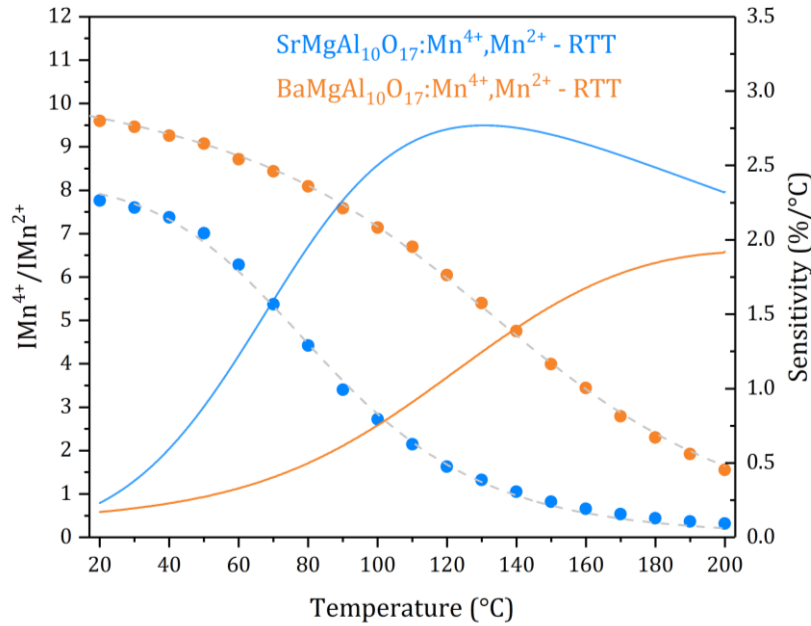


Figure 5 : Mn<sup>4+</sup>/Mn<sup>2+</sup> intensity ratios of SMA:Mn – RTT and BMA:Mn –RTT (dots), the dashed lines correspond to the fitting curves and the solid lines are the associated thermal sensitivities.

$$S = \left| \frac{\frac{1}{\frac{I_{Mn^{4+}}}{I_{Mn^{2+}}}}}{\frac{d}{dT} \left( \frac{I_{Mn^{4+}}}{I_{Mn^{2+}}} \right)} \right| \quad (3)$$

The evolution of  $Mn^{4+}/Mn^{2+}$  ratio according to the temperature is also investigated for SMA:Mn samples without RTT or with a higher temperature of RTT namely 800 °C (Figure SI - 5). The absolute value of the ratio changes according to the RTT temperature but the variation remains similar, as represented by the sensitivity curves. The maximal sensitivity occurs in the same temperature range (between 125 and 130 °C) and the maximal value is around 2.5 and 3 %/°C for the three samples. One interesting change is the difference in emission color range of the phosphor. The emission color obtained from CIE coordinates are represented in Figure 6. The horizontal bars represent the color evolution from RT (left) to high temperature (right). Whereas the SMA:Mn sample without RTT (Figure 6a) displays a color change from red to green with temperature increase up to 200 °C, the color range for SMA:Mn sample with a 750 °C RTT (Figure 6b) and 800 °C RTT (Figure 6c) present a different behavior. The temperature of color variation (i.e. temperature threshold) can also be tuned according to the temperature of the RTT. The resulting emission color changes from yellow to green around 125°C for SMA:Mn sample without RT, while the same phenomenon occurs at 90 °C and 70 °C for SMA:Mn sample with a 750°C and 800 °C RTT respectively (dashed lines Figure 6). This remarkable property can then be explored for temperature variation detection. Unlike the absolute and self-referenced determination of the temperature, which can be achieved thanks to  $Mn^{4+}/Mn^{2+}$  intensity ratio, the color change tracking will allow an accessible and simply-to-implement temperature identification around a temperature threshold. The color range as well as the temperature threshold can

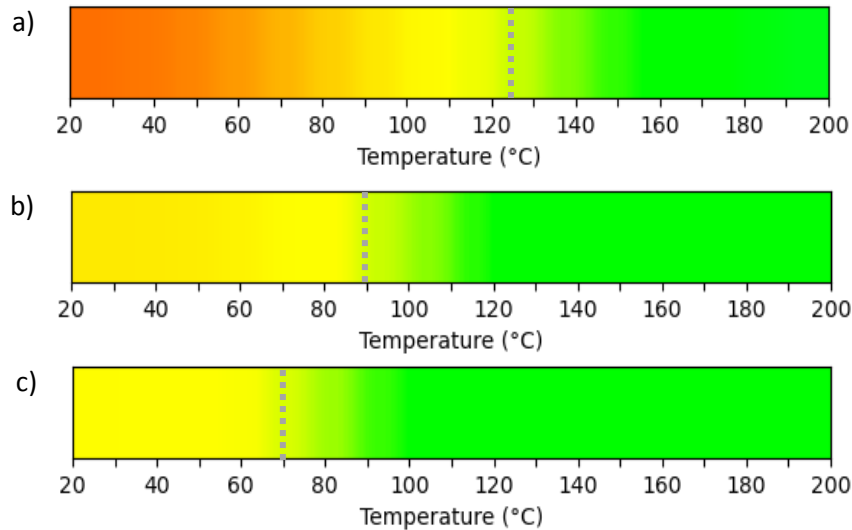


Figure 6 : Evolution of the resulting emitting color according to the temperature of a) SMA:Mn without RTT samples b) SMA:Mn-RTT 750 °C c) SMA:Mn-RTT 800 °C, threshold temperatures are reported in dashed lines.

be tuned for a single material according to the  $Mn^{4+}/Mn^{2+}$  ratio, and can be relevant for many applications as electronics or microfluidics, where critical temperature should not be exceeded for performances sustainability. Thus, after calibration, the same material can be used as dual mode thermometer, namely colorimetric and ratiometric.

The luminescence thermal stability is also investigated for  $BaMgAl_{10}O_{17}:Mn^{4+},Mn^{2+}$ -RTT sample (SI - 6). As reported in Figure 5, the  $Mn^{4+}/Mn^{2+}$  intensity ratio also decreases with temperature increase (orange dots). Nevertheless, the luminescence behavior of  $BaMgAl_{10}O_{17}:Mn^{4+},Mn^{2+}$ -RTT sample deviates from  $SMA:Mn$ -RTT one. It is important to notice that for both samples no irreversible change in the luminescence properties occurs with the temperature increase. Cyclic processes are performed between two temperatures (40 °C and 100 °C), showing the reversibility of the luminescence properties as well as the robustness of the thermal sensor (SI - 7). Following the Shannon and Prewitt table, the ionic radius of  $Sr^{2+}$  (resp.  $Ba^{2+}$ ) inserted in a 6-coordinated site is about 126 pm (resp. 142 pm). This difference in ionic radius leads to a change in crystal lattice parameters, the values obtained from Rietveld refinement are reported in SI - 2. Hence a remarkable change in luminescence properties is observed between  $SMA:Mn$ -RTT and  $BMA:Mn$ -RTT materials. Besides the blue shift of photoluminescence excitation spectrum of  $BMA:Mn$  reported in the previous part, the luminescence thermal stability is also influenced. Whereas only 31 % of initial  $Mn^{4+}$  intensity is detected at 100 °C for  $SMA:Mn$ -RTT, 66 % of initial  $Mn^{4+}$  intensity remains in  $BMA:Mn$ -RTT at the same temperature (Table 1). However, in the case of  $BMA:Mn$ , two different contributions should be taken into account in order to understand the intensity ratio evolution according to the temperature, identified as channel 2 and 3, indicating that unlike  $SAM:Mn$ -RTT, more than one quenching process occurs in  $BMA:Mn$ -RTT.

Temperature	<b>SrMgAl<sub>10</sub>O<sub>17</sub>:Mn<sub>0.2%at</sub> - RTT</b>		<b>BaMgAl<sub>10</sub>O<sub>17</sub>:Mn<sub>0.2%at</sub> - RTT</b>	
	<b>IMn<sup>2+</sup> vs I<sub>Tamb</sub></b>	<b>IMn<sup>4+</sup> vs I<sub>Tamb</sub></b>	<b>IMn<sup>2+</sup> vs I<sub>Tamb</sub></b>	<b>IMn<sup>4+</sup> vs I<sub>Tamb</sub></b>
<b>50 °C</b>	90 %	87 %	95 %	98 %
<b>100 °C</b>	78 %	31 %	89 %	66 %
<b>200 °C</b>	59 %	2 %	77 %	12 %

Table 1 : Intensity percentage at several temperatures compared to intensity at room temperature of  $Mn^{2+}$  and  $Mn^{4+}$  photoluminescence emission bands.

The fitting curve of  $Mn^{4+}/Mn^{2+}$  ratio in  $BMA$ -RTT material is plotted in dashed line in Figure 5 with the fitting parameters  $I_0 = 10.73 \pm 0.02$ ,  $a_2 = 560462 \pm 256072$ ,  $\Delta E_2 = 3825 \pm 143 \text{ cm}^{-1}$ ,  $a_3 = 9.7 \pm 2.9 \text{ cm}^{-1}$  and  $\Delta E_3 = 917 \pm 64 \text{ cm}^{-1}$ . The new deexcitation channel (channel 3) exhibits a lower activation energy of thermal quenching process ( $\Delta E_3$ ), and consequently occurs at lower temperature. Nevertheless,  $a_2 \gg a_3$ , meaning that the ratio of non-radiative vs. radiative transition probabilities is

much higher for the deexcitation channel with  $\Delta E_2 = 3825 \pm 143 \text{ cm}^{-1}$ . To this end, we assume that the deexcitation channel 2 can be considered as predominant. The maximal sensitivity of BMA:Mn-RTT arise at higher temperatures than SMA:Mn-RTT sample and reaches  $1.9 \text{ \%}/^\circ\text{C}$  at  $200 \text{ }^\circ\text{C}$ .

The difference in activation energies of thermal quenching process between  $\text{SrMgAl}_{10}\text{O}_{17}:\text{Mn}^{4+}, \text{Mn}^{2+}$ -RTT ( $\Delta E_1$ ) and  $\text{BaMgAl}_{10}\text{O}_{17}:\text{Mn}^{4+}, \text{Mn}^{2+}$ -RTT ( $\Delta E_2$ ) is directly linked to the crystal field energy. To illustrate this statement, the energy level diagram is reported in Figure 7. In both materials,  ${}^2\text{E} \rightarrow {}^4\text{A}_2$  transition is responsible of  $\text{Mn}^{4+}$  red luminescence. Excitations at 426 and 450 nm for SMA:Mn and BMA:Mn materials respectively allow the promotion of electron from the  ${}^4\text{A}_2$  ground state to the  ${}^4\text{T}_2$  excited state. The presence of an intersection between parabolas of the ground state and excited states induces a non-radiative deexcitation channel. Thus  $\Delta E$  value calculated using the Mott-Seitz model, can be defined as the energy difference between the  ${}^2\text{E}$  emitting level and the cross-intersection point. With temperature increase, the probability of non-radiative deexcitation through this channel increases, and above a certain temperature, this deexcitation path prevails. As illustrated by the Tanabe-Sugano diagram, no change occurs in the relative position between the  ${}^4\text{A}_2$  ground state and the  ${}^2\text{E}$  excited level according to the crystal field. However, the position of the  ${}^4\text{T}_2$  level shifts toward higher energy with crystal field increase. Thus, the crossover responsible for the non-radiative deexcitation process occurs between the parabolas of the  ${}^4\text{A}_2$  ground state and the  ${}^4\text{T}_2$  excited state. As a consequence, the activation energies of thermal quenching process increase in BMA:Mn-RTT ( $\Delta E_2 = 3825 \pm 143 \text{ cm}^{-1}$ ) relatively to SMA:Mn-RTT material ( $\Delta E_1 = 3696 \pm 139 \text{ cm}^{-1}$ ). Thus the crystal field splitting drastically influences the luminescence thermal stability of  $\text{Mn}^{4+}$ -doped material and shifts the maximal thermal sensitivity to higher temperature. By modulating the environment of the activator, the temperature range on which the thermal sensor is efficient can then be adjusted.

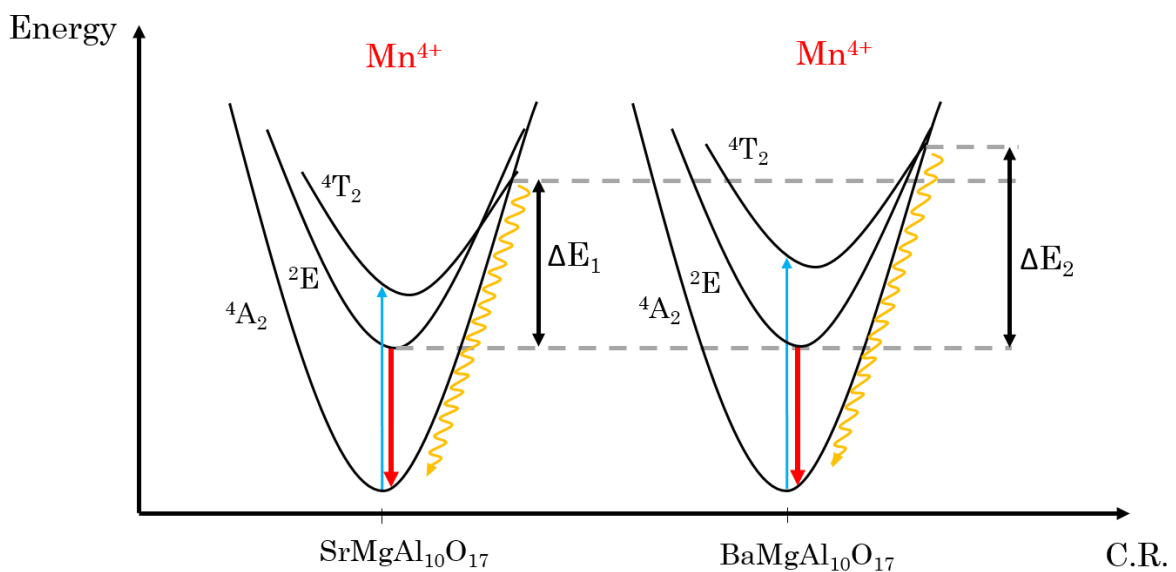


Figure 7 : Energy levels diagram of  $\text{Mn}^{4+}$  ion inserted in  $\text{SrMgAl}_{10}\text{O}_{17}$  and  $\text{BaMgAl}_{10}\text{O}_{17}$  hosts.

## 4. Conclusion

In summary, the co-stabilization of Mn ions with two different valence states have been highlighted from the analysis of photoluminescence properties. The proportion of each valence states of dopant have been finely controlled according to the temperature variation of the reductive post-treatment. We developed a strategy, allowing to synthesize and analyze the properties of multiple samples in a combinatorial approach and demonstrate the possibility of a fast and thorough tuning of the luminescence properties. Furthermore, we also evidenced the ability of SMA:Mn and BMA:Mn materials doped with Mn<sup>4+</sup> and Mn<sup>2+</sup> activators as competitive and reliable dual-mode luminescent thermometers (colorimetric and ratiometric). The valence state of dopant as well as the crystal field of the host have been demonstrated as critical parameters, that can be simply tuned in order to optimize the thermal response of the sensor and control the temperature range on which the thermometer is efficient. This strategy can then be adapted to other thermometers in order to accelerate their luminescence properties optimization, and can be generalized to other applications as LEDs, imaging or anticounterfeiting.

## Declaration of competing interest

The authors declare that they have no known competing financial interests or personal relationships that could have appeared to influence the work reported in this paper.

## Acknowledgments

This work was supported by the National Agency for Research (ANR JCJC Combi-SSL, ANR-16-CE08-003-01).

## Appendix A : Supplementary material

Supplementary Material.

## References

- [1] M.D. Dramićanin, Trends in luminescence thermometry, *Journal of Applied Physics*. 128 (2020) 040902. <https://doi.org/10.1063/5.0014825>.
- [2] F. Vetrone, R. Naccache, A. Zamarrón, A. Juarraz de la Fuente, F. Sanz-Rodríguez, L. Martínez Maestro, E. Martín Rodríguez, D. Jaque, J. García Solé, J.A. Capobianco, Temperature Sensing Using Fluorescent Nanothermometers, *ACS Nano*. 4 (2010) 3254–3258. <https://doi.org/10.1021/nn100244a>.
- [3] C.D.S. Brites, P.P. Lima, N.J.O. Silva, A. Millán, V.S. Amaral, F. Palacio, L.D. Carlos, Thermometry at the nanoscale, *Nanoscale*. 4 (2012) 4799. <https://doi.org/10.1039/c2nr30663h>.
- [4] R. G. Geitenbeek, J. C. Vollenbroek, H.M. H. Weijgertze, C.B. M. Tregouet, A.-E. Nieuwelink, C. L. Kennedy, B. M. Weckhuysen, D. Lohse, A. van Blaaderen, A. van den Berg, M. Odijk, A. Meijerink, Luminescence thermometry for in situ temperature measurements in microfluidic devices, *Lab on a Chip*. 19 (2019) 1236–1246. <https://doi.org/10.1039/C8LC01292J>.
- [5] E.J. McLaurin, L.R. Bradshaw, D.R. Gamelin, Dual-Emitting Nanoscale Temperature Sensors, *Chemistry of Materials*. 25 (2013) 1283–1292. <https://doi.org/10.1021/cm304034s>.
- [6] M.D. Dramićanin, Sensing temperature via downshifting emissions of lanthanide-doped metal oxides and salts. A review, *Methods and Applications in Fluorescence*. 4 (2016) 042001. <https://doi.org/10.1088/2050-6120/4/4/042001>.
- [7] L. Marciniak, K. Trejgis, Luminescence lifetime thermometry with  $Mn^{3+}$ – $Mn^{4+}$  co-doped nanocrystals, *Journal of Materials Chemistry C*. 6 (2018) 7092–7100. <https://doi.org/10.1039/C8TC01981A>.
- [8] Q. Zhou, L. Dolgov, A. M. Srivastava, L. Zhou, Z. Wang, J. Shi, M. D. Dramićanin, M. G. Brik, M. Wu,  $Mn^{2+}$  and  $Mn^{4+}$  red phosphors: synthesis, luminescence and applications in WLEDs. A review, *Journal of Materials Chemistry C*. 6 (2018) 2652–2671. <https://doi.org/10.1039/C8TC00251G>.
- [9] M.G. Brik, S.J. Camardello, A.M. Srivastava, Influence of Covalency on the  $Mn^{4+} 2E_g \rightarrow 4A_{2g}$  Emission Energy in Crystals, *ECS J. Solid State Sci. Technol.* 4 (2014) R39. <https://doi.org/10.1149/2.0031503jss>.
- [10] Z. Zhou, N. Zhou, M. Xia, M. Yokoyama, H.T. (Bert) Hintzen, Research progress and application prospects of transition metal  $Mn^{4+}$ -activated luminescent materials, *J. Mater. Chem. C*. 4 (2016) 9143–9161. <https://doi.org/10.1039/C6TC02496C>.
- [11] Y. Li, S. Qi, P. Li, Z. Wang, Research progress of Mn doped phosphors, *RSC Advances*. 7 (2017) 38318–38334. <https://doi.org/10.1039/C7RA06026B>.
- [12] S.-H. Yang, Y.-C. Lee, Y.-C. Hung, Thermometry of red nanoflaked  $SrAl_{12}O_{19}:Mn^{4+}$  synthesized with boric acid flux, *Ceramics International*. 44 (2018) 11665–11673. <https://doi.org/10.1016/j.ceramint.2018.03.242>.
- [13] E. Glais, V. Đorđević, J. Papan, B. Viana, M.D. Dramićanin,  $MgTiO_3:Mn^{4+}$  a multi-reading temperature nanoprobe, *RSC Adv.* 8 (2018) 18341–18346. <https://doi.org/10.1039/C8RA02482K>.
- [14] M.D. Dramićanin, B. Milićević, V. Đorđević, Z. Ristić, J. Zhou, D. Milivojević, J. Papan, M.G. Brik, C.-G. Ma, A.M. Srivastava, M. Wu,  $Li_2TiO_3:Mn^{4+}$  Deep-Red Phosphor for the Lifetime-Based Luminescence Thermometry, *ChemistrySelect*. 4 (2019) 7067–7075. <https://doi.org/10.1002/slct.201901590>.
- [15] K. Trejgis, M.D. Dramićanin, L. Marciniak, Highly sensitive multiparametric luminescent thermometer for biologically-relevant temperatures based on  $Mn^{4+}$ ,  $Ln^{3+}$  co-doped  $SrTiO_3$  nanocrystals, *Journal of Alloys and Compounds*. 875 (2021) 159973. <https://doi.org/10.1016/j.jallcom.2021.159973>.
- [16] L. Dong, L. Zhang, Y. Jia, Y. Xu, S. Yin, H. You,  $ZnGa_{2-y}Al_yO_4:Mn^{2+}, Mn^{4+}$  Thermo-chromic Phosphors: Valence State Control and Optical Temperature Sensing, *Inorg. Chem.* 59 (2020) 15969–16976. <https://doi.org/10.1021/acs.inorgchem.0c02474>.

- [17] Y. Zhu, C. Li, D. Deng, B. Chen, H. Yu, H. Li, L. Wang, C. Shen, X. Jing, S. Xu, A high-sensitivity dual-mode optical thermometry based on one-step synthesis of  $\text{Mn}^{2+}:\text{BaAl}_{12}\text{O}_{19}-\text{Mn}^{4+}:\text{SrAl}_{12}\text{O}_{19}$  solid solution phosphors, *Journal of Alloys and Compounds*. 853 (2021) 157262. <https://doi.org/10.1016/j.jallcom.2020.157262>.
- [18] G. Ju, Y. Hu, L. Chen, X. Wang, Photoluminescence properties of color-tunable  $\text{SrMgAl}_{10}\text{O}_{17}:\text{Eu}^{2+},\text{Mn}^{2+}$  phosphors for UV LEDs, *Journal of Luminescence*. 132 (2012) 1792–1797. <https://doi.org/10.1016/j.jlumin.2012.02.036>.
- [19] R. Cao, H. Xue, X. Yu, F. Xiao, D. Wu, F. Zhang, Luminescence Properties and Synthesis of  $\text{SrMgAl}_{10}\text{O}_{17}:\text{Mn}^{4+}$  Red Phosphor for White Light-Emitting Diodes, (2016). <https://doi.org/info:doi/10.1166/jnn.2016.11793>.
- [20] V. Singh, G. Sivaramaiah, J.L. Rao, N. Singh, A.K. Srivastava, H.D. Jirimali, J. Li, H. Gao, R.S. Kumaran, P.K. Singh, S.J. Dhoble,  $\text{Eu}^{2+}$  and  $\text{Mn}^{2+}$  Co-doped  $\text{BaMgAl}_{10}\text{O}_{17}$  Blue- and Green-Emitting Phosphor: A Luminescence and EPR Study, *Journal of Elec Materi*. 45 (2016) 2776–2783. <https://doi.org/10.1007/s11664-016-4370-3>.
- [21] B. Wang, H. Lin, F. Huang, J. Xu, H. Chen, Z. Lin, Y. Wang, Non-Rare-Earth  $\text{BaMgAl}_{10-2x}\text{O}_{17}:\text{xMn}^{4+},\text{xMg}^{2+}$ : A Narrow-Band Red Phosphor for Use as a High-Power Warm w- LED, *Chem. Mater*. 28 (2016) 3515–3524.
- [22] R. Cao, Y. Ye, Q. Peng, S. Guo, Z. Hu, W. Hu, H. Ao, X. Yu, Luminescence properties and charge compensation of  $\text{BaMgAl}_{10}\text{O}_{17}:\text{Mn}^{4+}$ , K red emitting phosphor, *Optoelectronics and Advanced Materials - Rapid Communications*. 12 (2018) 71–75.
- [23] Y. Xu, L. Wang, B. Qu, D. Li, J. Lu, R. Zhou, The role of co-dopants on the luminescent properties of  $\alpha\text{-Al}_2\text{O}_3:\text{Mn}^{4+}$  and  $\text{BaMgAl}_{10}\text{O}_{17}:\text{Mn}^{4+}$ , *Journal of the American Ceramic Society*. 102 (2019) 2737–2744. <https://doi.org/10.1111/jace.16155>.
- [24] J. Hu, E. Song, Y. Zhou, S. Zhang, S. Ye, Z. Xia, Q. Zhang, Non-stoichiometric defect-controlled reduction toward mixed-valence Mn-doped hexaaluminates and their optical applications, *Journal of Materials Chemistry C*. 7 (2019) 5716–5723. <https://doi.org/10.1039/C9TC01026B>.
- [25] H. Kang, K.N. Lee, S. Unithrattil, H.J. Kim, J.H. Oh, J.S. Yoo, W.B. Im, Y.R. Do, Narrow-Band  $\text{SrMgAl}_{10}\text{O}_{17}:\text{Eu}^{2+},\text{Mn}^{2+}$  Green Phosphors for Wide-Color-Gamut Backlight for LCD Displays, *ACS Omega*. 5 (2020) 19516–19524. <https://doi.org/10.1021/acsomega.0c01798>.
- [26] G. Kaur Behrh, H. Serier- Brault, S. Jobic, R. Gautier, A Chemical Route Towards Single-Phase Materials with Controllable Photoluminescence, *Angewandte Chemie*. 127 (2015) 11663–11665. <https://doi.org/10.1002/ange.201504224>.
- [27] H. Yuan, R. Génois, E. Glais, F. Chen, Q. Shen, L. Zhang, E. Faulques, F. Massuyeau, R. Gautier, Tuning the oxidation states of dopants in  $\text{Li}_2\text{SrSiO}_4:\text{Eu},\text{Ce}$  and control of the photoemission color, *Journal of Solid State Chemistry*. 288 (2020) 121367. <https://doi.org/10.1016/j.jssc.2020.121367>.
- [28] S. Adachi, Photoluminescence properties of  $\text{Mn}^{4+}$ -activated oxide phosphors for use in white-LED applications: A review, *Journal of Luminescence*. 202 (2018) 263–281. <https://doi.org/10.1016/j.jlumin.2018.05.053>.
- [29] S. Adachi, Crystal-field and Racah parameters of  $\text{Mn}^{4+}$  ion in red and deep red-emitting phosphors: Fluoride versus oxide phosphor, *Journal of Luminescence*. 218 (2020) 116829. <https://doi.org/10.1016/j.jlumin.2019.116829>.
- [30] C.D.S. Brites, A. Millán, L.D. Carlos, Chapter 281 - Lanthanides in Luminescent Thermometry, in: J.-C. Bunzli, V. K. Pecharski (Eds.), *Handbook on the Physics and Chemistry of Rare Earths*, Elsevier, 2016: pp. 339–427. <https://doi.org/10.1016/bs.hpre.2016.03.005>.
- [31] X. Wang, O.S. Wolfbeis, R.J. Meier, Luminescent probes and sensors for temperature, *Chemical Society Reviews*. 42 (2013) 7834. <https://doi.org/10.1039/c3cs60102a>.
- [32] M. Dramićanin, *Luminescence Thermometry: Methods, Materials, and Applications*, Woodhead Publishing, 2018.